Matter

CellPress

Article

Epitaxial Dimers and Auger-Assisted Detrapping in PbS Quantum Dot Solids

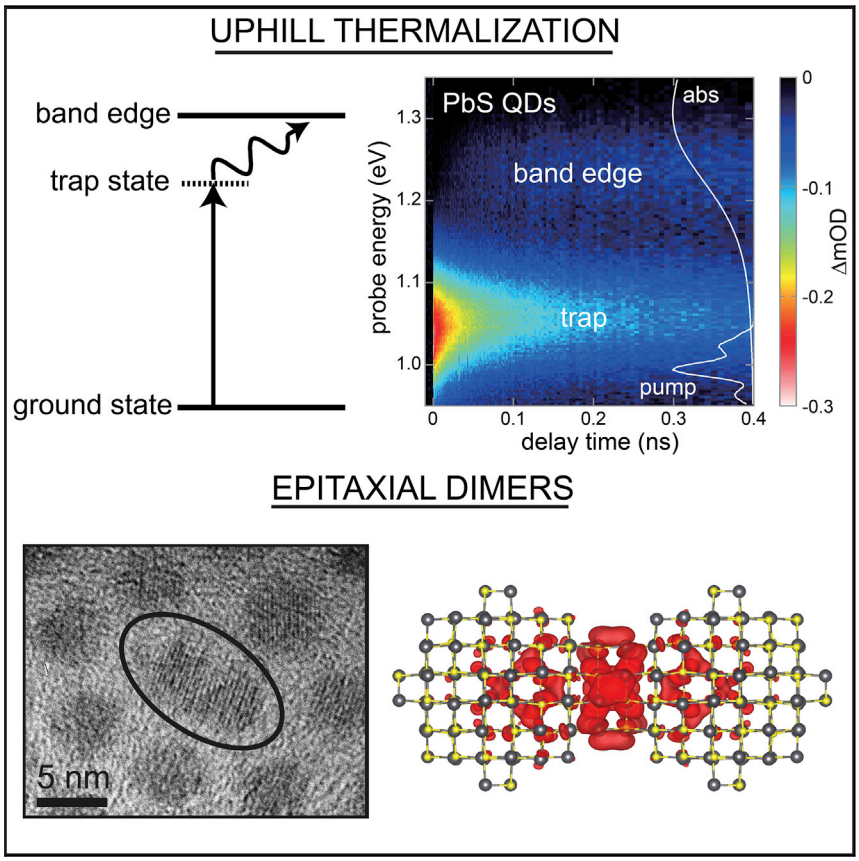

Time-resolved laser spectroscopy was used to measure the dynamics of charge-carrier trapping and detrapping in PbS quantum dot solids. These measurements, together with electron microscopy and numerical simulations, point toward fused quantum dot dimers as the primary source of optically active trap states in PbS quantum dot solids.

Rachel H. Gilmore, Yun Liu, Wenbi Shcherbakov-Wu, ..., Adam P. Willard, Jeffrey C. Grossman, William A. Tisdale

tisdale@mit.edu

HIGHLIGHTS

Epitaxial dimers are the primary optically active trap state in PbS QD solids

Transient absorption reveals trapping and detrapping kinetics

Uphill thermalization of trapped charge carriers is entropically driven

An Auger-assisted detrapping pathway is active at higher carrier density

Benchmark
First qualification/assessment of material properties and/or performance

Gilmore et al., Matter 1, 250–265
July 10, 2019
https://doi.org/10.1016/j.matt.2019.05.015

Matter

CellPress

Article

Epitaxial Dimers and Auger-Assisted Detrapping in PbS Quantum Dot Solids

Rachel H. Gilmore,[1] Yun Liu,[2] Wenbi Shcherbakov-Wu,[4] Nabeel S. Dahod,[1] Elizabeth M.Y. Lee,[1] Mark C. Weidman,[1] Huashan Li,[2] Joel Jean,[3] Vladimir Bulović,[3] Adam P. Willard,[4] Jeffrey C. Grossman,[2] and William A. Tisdale[1,5,*]

SUMMARY

We explore the dynamic interaction of charge carriers between band-edge states and sub-band trap states in PbS quantum dot (QD) solids using time-resolved spectroscopy. In monodisperse arrays of 4- to 5-nm diameter PbS QDs, we observe an optically active trap state ~100–200 meV below the band edge that occurs at a frequency of 1 in ~2,500 QDs. Uncoupled QD solids with oleic acid ligands show trap-to-ground-state recombination that resembles Auger recombination. In electronically coupled QD solids, we observe entropically driven uphill thermalization of trapped charge carriers from the trap state to the band edge via two distinct mechanisms: Auger-assisted charge transfer (~35 ps) and thermally activated hopping (~500 ps). Photophysical characterization combined with atomistic simulations and high-resolution electron microscopy suggest that these states arise from epitaxially fused pairs of QDs rather than electron or hole traps at the QD surface, offering new strategies for improving the optoelectronic performance of QD materials.

INTRODUCTION

Colloidal nanocrystal quantum dots (QDs) are promising building blocks for next-generation optoelectronic technologies because of their tunable size and shape, size-dependent optical properties, and flexible ligand chemistry. However, challenges associated with the synthesis and formation of electronically coupled QD solids remain.[1,2] In particular, mid-band-gap trap states have garnered substantial attention because they limit photovoltaic device efficiencies by reducing the open-circuit voltage[3] and acting as charge-carrier recombination sites.[4] Trap states are involved in charge-carrier transport, either directly through mid-gap transport[5,6] or through multiple trapping and release steps.[7,8] The electronic characteristics of trap states are observed to vary with ligand treatments,[9,10] air exposure,[11] and other oxidation treatments,[12] prompting speculation that trap states are associated with structural defects or unpassivated sites on the QD surface, or with strongly coupled QD aggregates.[1,4,13,14]

Here, we use broadband near-infrared transient absorption (TA) spectroscopy to study the dynamics of charge-carrier detrapping in PbS QD solids. By employing highly monodisperse QDs (size dispersity 1%–3%), we are able to spectrally distinguish the trap state from the normal inhomogeneous distribution of band-edge states. In electronically coupled QD solids, we observe efficient uphill thermalization of trapped charge carriers to the band-edge transport level. Detrapping is entropically favored due to the large excess density of band-edge states relative to trap states. We observe two kinetic mechanisms of detrapping: (1) a fluence-dependent,

Progress and Potential

Colloidal quantum dots (QDs) are solution-processable semiconductor nanomaterials that have found use in television displays, photodetectors, light-emitting devices, lasers, and solar cells. However, electrical charge transport through QD arrays is limited by the frequent encounter of charges with "trap states," electronic defects that disrupt charge transport. Previously, these states were thought to arise from structural defects on nanocrystal surfaces. Here, we show that the photophysical characteristics of optically active trap states in PbS QD solids suggest that their most likely origin is epitaxial dimers—two QDs that have fused together with a continuous crystal structure. We use ultrafast spectroscopy to measure the dynamic interactions of charges with these states and demonstrate a novel detrapping mechanism. These dimer states are likely created during ligand exchange, creating challenges for the development of high-efficiency QD optoelectronic devices.

temperature-independent Auger-assisted electron transfer process that occurs on a time scale of ~35 ps, and (2) a fluence-independent, temperature-dependent, thermally assisted hopping process that occurs on a time scale of ~500 ps at room temperature. From temperature-dependent photoluminescence (PL) measurements, we infer a trap-state density of 1 in ~2,500 QDs, which is consistent with literature reports for thiol-treated QD solids.[10,11,15] In addition, we use kinetic Monte Carlo (KMC) simulations to confirm the entropically driven charge-carrier detrapping mechanism.

Upon direct photoexcitation of the trap state in QD solids with insulating oleic acid ligand, we observe clear signatures of Auger recombination, revealing a trap-state degeneracy, biexciton decay time, and absorption cross-section similar to the band-edge state of a single QD, rather than an electron or hole surface trap. Transmission electron microscopy (TEM) image analysis confirms the absence of unusually large QDs but also reveals the infrequent occurrence of epitaxially fused QD dimers, which can explain our findings. Strong electronic coupling between two fused QDs can generate new states lower in energy by ~100–200 meV relative to the single QD band gap[14,16] (1.08 eV for 4.9-nm diameter QDs and 1.3 eV for 4.2-nm diameter QDs, as studied here). Furthermore, density functional theory (DFT) calculations of PbS QD dimers epitaxially attached on the (100) facet exhibit optical properties and energy shifts that are consistent with spectroscopic results.

Direct Photoexcitation of the Trap State

PbS QDs were synthesized via the $PbCl_2$ method according to previously published procedures,[17,18] dispersed in toluene, and spin coated onto glass substrates for TA measurements or single crystal quartz substrates for temperature-dependent PL measurements. To make electronically coupled solids, we ligand-exchanged QD films with ethanethiol in a nitrogen glovebox (see Experimental Procedures).[19]

To probe charge-carrier detrapping kinetics, we performed experiments in which we directly photoexcited the ground-to-trap-state transition using a sub-band-gap laser pulse, and subsequently tracked the dynamic occupation of the trap and band-edge states using ultrafast TA spectroscopy (Figure 1A and Experimental Procedures). In Figure 1B, the trap state at 1.06 eV of 4.2-nm diameter (1.3 eV) QDs is excited with a 0.99-eV pump laser pulse. Immediately following photoexcitation, only the trap state is occupied. The band-edge bleach feature subsequently grows in over the next ~500 ps as the intensity of the trap-state bleach feature decreases, signaling population transfer from trap to band edge. Spectral slices (Figure 1C) clearly show only the trap-state bleach at early times, and the population of both states at later times. The energy of the band-edge bleach signal at 1.24 eV is the same as the thermalized energy of the band-edge TA signal when excited well above the band gap.[20] The integrated intensities of the band-edge and trap-state bleach features as a function of time are shown in Figure 1D. By ~2.0 ns, equilibrium between the trap state and the band edge has been reached and the ratio of the intensity of the two bleach features subsequently remains constant. If we assume that the decrease in bleach intensity of the trap state is entirely due to carriers detrapping to the band-edge state, we estimate that the trap-state absorption cross-section is approximately two to three times greater than the band-edge absorption cross-section.

The behavior shown in Figure 1 is characteristic of an entropically driven detrapping process. If the density of states at the band edge is much larger than the density of

[1]Department of Chemical Engineering, Massachusetts Institute of Technology, Cambridge, MA 02139, USA

[2]Department of Materials Science and Engineering, Massachusetts Institute of Technology, Cambridge, MA 02139, USA

[3]Department of Electrical Engineering and Computer Science, Massachusetts Institute of Technology, Cambridge, MA 02139, USA

[4]Department of Chemistry, Massachusetts Institute of Technology, Cambridge, MA 02139, USA

[5]Lead Contact

*Correspondence: tisdale@mit.edu

https://doi.org/10.1016/j.matt.2019.05.015

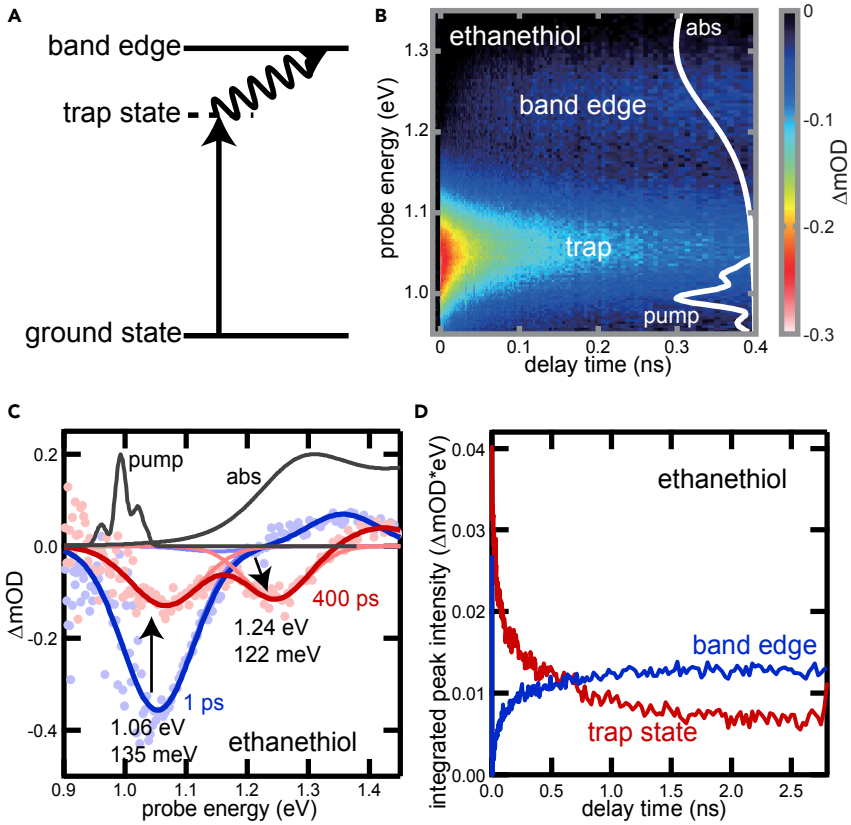

Figure 1. Uphill Thermalization of Trapped Charge Carriers

(A) Energy-level diagram showing direct excitation of the trap state followed by uphill thermalization to the band edge.

(B) TA color plot showing spectral dynamics following excitation of the trap state in QD solids (d = 4.2 nm, δ = 2.1–3.0%) as a function of ligand length. The pump spectra and QD solution absorption spectra are overlaid as solid white lines for reference.

(C) Selected TA spectra at 1 ps and 400 ps following photoexcitation of the trap state shown in (B).

(D) Integrated peak intensities as a function of delay time for the ethanethiol-treated solid shown in (B).

trap states $\left(\frac{DOS_{BE}}{DOS_{trap}} > e^{(-E_{BE}-E_{trap})/k_B T}\right)$, then charge carriers are more likely to be found at the band edge than the trap level once equilibrium is reached. In this case, entropy maximization drives charge carriers uphill in energy.

It is noteworthy that when the trap state is selectively excited, no bleach signal is observed initially at the band-edge energy. The conduction and valence band edges have the same degeneracy in lead chalcogenide QDs, so the electrons and holes contribute approximately equally to the TA band-edge bleach signal.[21] The absence of a bleach feature at the band-edge energy implies that the excitation does not involve an electron or hole in a core band-edge level of a typical QD (for instance, a transition from a band-edge level to an empty surface state), which would immediately contribute a partial bleach at the band-edge energy.

Spectral signatures of the trap state are also observed in QD solids with oleic acid ligands, but uphill thermalization to the band edge does not occur (Figure 2E). Exciting the trap state in QD solids with varying-length thiol ligands (Figures 2A–2D),

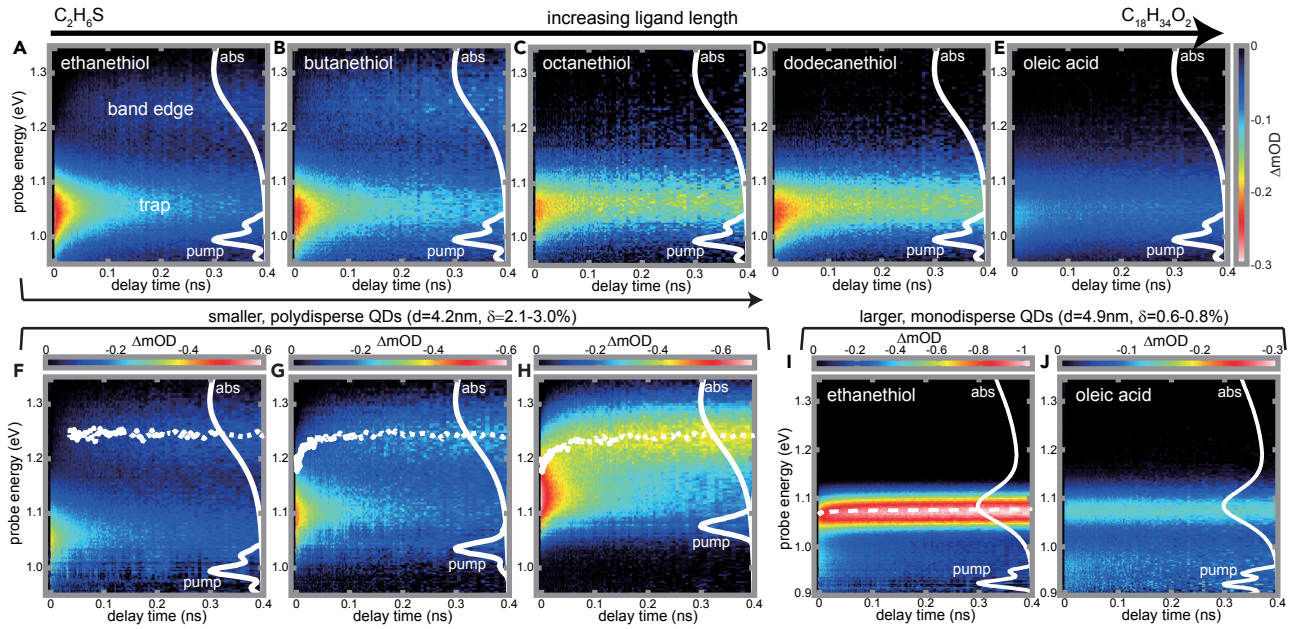

Figure 2. Spectral Dynamics following Direct Photoexcitation of the Trap State at 300 K

(A–E) TA color plots showing spectral dynamics following excitation of the trap state in QD solids (d = 4.2 nm, δ = 2.1–3.0%) as a function of ligand length: (A) ethanethiol, (B) butanethiol, (C) octanethiol, (D) dodecanethiol, (E) oleic acid (ligands are indicated above plots). The pump spectra and QD solution absorption spectra are overlaid as solid white lines for reference. (A) is a replica of (B) from Figure 1.

(F–H) TA color plots showing spectral dynamics as the excitation wavelength is tuned closer to the band edge (increasing energy; pump spectra indicated by solid white line): (F) excitation at 0.99 eV, (G) excitation at 1.03 eV, (H) excitation at 1.08 eV.

(I and J) TA color plots showing spectral dynamics in larger, more monodisperse QD solids (d = 4.9 nm, δ = 0.6–0.8%) whose band-edge absorption peak is near the homogeneous limit: (I) ethanethiol, (J) oleic acid. The laser excitation pulse is sufficiently broad to excite both the trap state and the band-edge state.

See also Figures S1–S4, S7, and S8.

we see that detrapping occurs only for the shortest two ligands, ethanethiol and butanethiol, but not for the longer octanethiol or dodecanethiol ligands. From these results, we conclude that electronic coupling and fast diffusion away from the trap site is needed to depopulate the trap state (see also Figure S1). Additionally, we note that the trap-state bleach intensity in the thiol-treated samples is consistently ~3-fold greater than that in the oleic acid sample, indicating an increase in the trap-state density following ligand exchange.

To gain a better understanding of the energy distribution of the trap state as compared with the band-edge state, we vary the excitation wavelength in the ethanethiol QD solid. As the excitation energy is increased from 0.99 eV (Figure 2F) to 1.03 eV (Figure 2G) and 1.08 eV (Figure 2H), the excitation pulse begins to overlap with the low energy tail of the QD size distribution (Figure S2). The expected blue-shift of charge carriers in the band-edge manifold toward the thermalized equilibrium average energy (white dashed line) is then observed in addition to depopulation of the trap state.

Similar behavior is also observed in more monodisperse ensembles of larger-sized QDs (4.9 nm, 1.08 eV), but the trap state and band-edge state are too close in energy to be selectively excited with our femtosecond laser excitation pulses (Figures 2I, 2J, and S2). However, two spectrally distinct features are observed in the TA spectrum for both the oleic acid-capped QDs and the thiol-exchanged QDs. The monodispersity of this QD batch (spectrally narrow band-edge bleach feature allowing clear separation

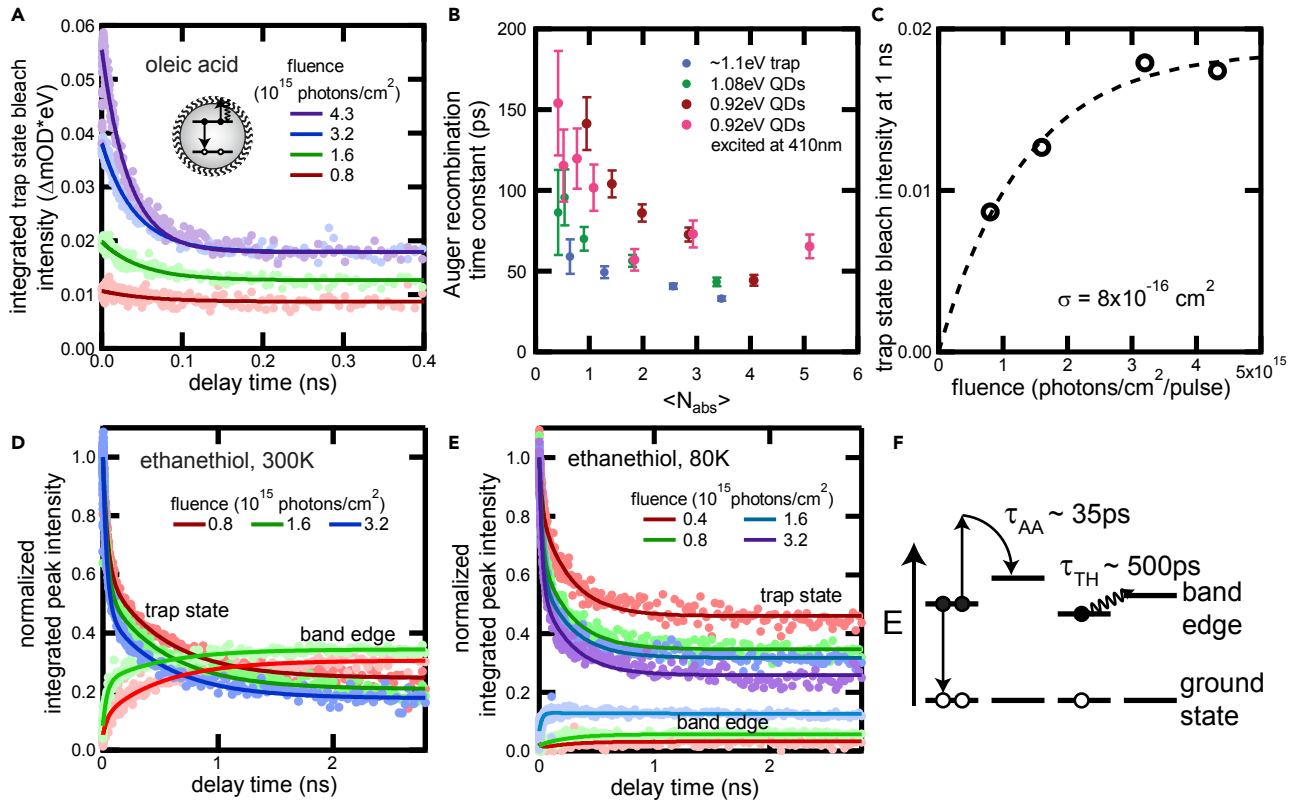

Figure 3. Analysis of Detrapping Kinetics

(A) Trap-state bleach intensity in QD solid with oleic acid ligands as a function of delay time, and excitation power showing dynamics characteristic of Auger recombination.

(B) Trap-state decay time constant in oleic acid-capped QDs as a function of number of excitons absorbed per QD, and comparison with Auger recombination in QDs with similar band-gap energy. Error bars represent uncertainty in the fitted fast-decay time component.

(C) Bleach intensity at 1 ns as a function of excitation fluence. Experimental data are shown as open circles, and a model fit to determine the absorption cross-section is shown by the dashed line. See also Figure S5.

(D and E) Comparison of trap-state and band-edge bleach dynamics in ethanethiol-treated QD solid as a function of trap-state excitation fluence at (D) 300 K and at (E) 80 K.

(F) Schematic showing two observed detrapping mechanisms. AA, Auger-assisted; TH, thermally activated.

from the trap-state feature) and the excitation energy dependence shown in Figures 2F–2H clearly demonstrate that the trap state is a distinct state and not simply the tail of the size distribution.[22,23] We also performed photothermal deflection spectroscopy, which showed continuous absorption in the sub-band-gap region, consistent with the existence of separate manifold of trap states (Figure S3).[24] Furthermore, the trap-state absorption bleach at 0.97 eV in these larger QDs is lower in energy than in the smaller QDs, and closer in energy to the band-edge peak (shallower depth), indicating a size dependence of the trap-state energy (Figure S2). We also note that these trap states are observed with other common ligands, such as 3-mercaptopropionic acid or tetrabutylammonium iodide (Figure S4), further indicating that they are a property of the QD solid and not specific to any surface treatment.

Kinetics of Detrapping

To learn more about the nature of the trap state and the detrapping process, we turn to analysis of the detrapping and recombination kinetics. Figure 3A presents the integrated trap-state bleach intensity in an oleic acid QD solid as a function of delay time following trap-state excitation for several different laser fluences. In this

sample, only trap-to-ground-state recombination is observed because QD-QD electronic coupling is too weak for uphill thermalization, which requires carrier transport away from the trapping site. The initial bleach intensity increases with fluence, as does the fraction of the intensity that decays within the first ~100 ps. These dynamics are reminiscent of Auger recombination dynamics[25] in isolated QDs in solution (Figure S5A). Indeed, the time constants of the multi-exciton decay are in line with the band-edge multi-exciton decay in PbS QDs (Figure 3B), which becomes faster for smaller QDs.[25] The absorption cross-section of the trap state can be estimated from the intensity-dependent measurements, and yields a value of 8×10^{-16} cm^2 (Figure 3C), which is the same order of magnitude as the band-edge state (Figures S5B and S5C).[26,27] Thus, based on their photophysical properties, the trap states behave much more like large QDs than like charge-separated surface defects.

Detrapping kinetics in electronically coupled QD solids (Figures 3D and 3E) resemble dynamics one might expect for larger QDs in a matrix of smaller QDs. Figure 3D presents the normalized integrated trap and band-edge bleach intensities as a function of delay time following direct trap-state excitation for different excitation fluences at 300 K. The decay of the trap signal and growth of the band-edge signal mirror each other, as expected for population transfer from the trap state manifold to the band edge. As the excitation fluence increases, the magnitude of population transfer from the trap to the band-edge state increases.

The detrapping process follows two time scales, with a fast component that increases in magnitude with increasing fluence and a slow component that does not depend on fluence. Fluence-dependent measurements at 80 K (Figure 3E) freeze out the slow detrapping mechanism, but reveal that the fast detrapping mechanism is temperature independent. The fast (~35 ps) detrapping process occurs on similar time scales as the Auger recombination process observed in oleic acid QD solids, suggesting that the temperature-independent, fluence-dependent fast detrapping process is an Auger-assisted electron transfer event.[28,29] As illustrated in Figure 3F, when two excitons occupy the same trap site, Auger recombination can generate a single energetic (hot) charge carrier, which is able to rapidly transfer to a neighboring QD before cooling back to the band edge. We assign the slower (~500 ps) detrapping mechanism to thermally activated charge-carrier hopping.[20] A summary of these two detrapping mechanisms is presented in Figure 3F.

Notably, at 80 K and low excitation fluence, where the Auger-assisted mechanism is not active and thermally activated detrapping is not observed (red traces, Figure 3E), decay of the trap-state bleach intensity is still observed even in the absence of growth of the band-edge signal. Within the 3-ns measurement window, ~50% of the trap-state population has decayed back to the ground state, indicating that the trap states we observe spectroscopically are possible recombination centers that negatively affect QD device efficiencies.

Quantum Dot Dimers Are a Source of Trap States

While the photophysical behavior of the trap state closely resembles that of larger QDs, the presence of anomalously large QDs within the ensemble is not supported by materials characterization. The PbS QDs used in this study are highly monodisperse,[17] with the standard deviation of the mean diameter estimated to be only 3.0% for the 4.2-nm QDs and 1.0% for the 4.9-nm QDs.[20] If the trap states were due to abnormally large QDs in the ensemble, the measured trap-state energies would correspond to QDs with diameters of 4.7 nm for the 4.2-nm batch and 5.4 nm for the 4.9-nm batch, which is 5–10 standard deviations away from the

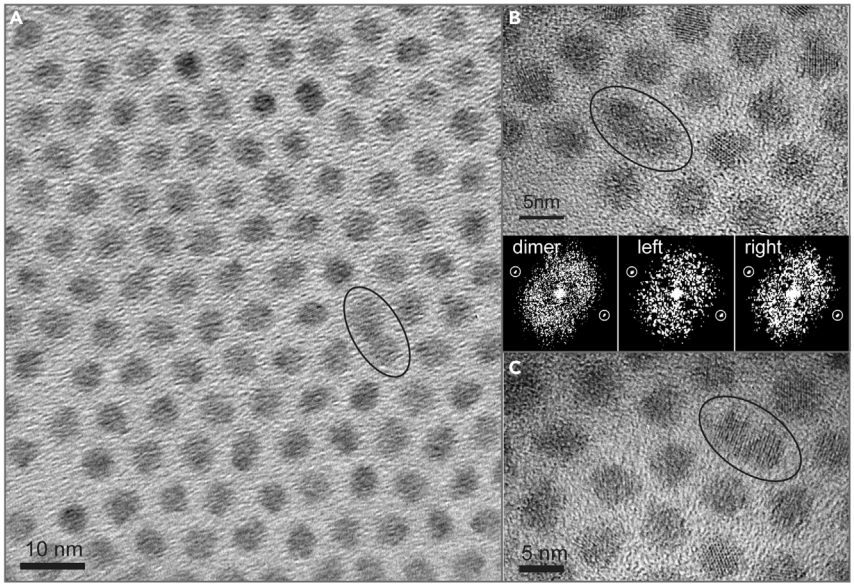

Figure 4. TEM Analysis of Epitaxially Fused QD Dimers

(A) TEM micrograph of monodisperse 4.9-nm QDs with oleic acid ligands showing an absence of anomalously large QDs but the presence of a QD dimer.

(B) HRTEM micrograph of an epitaxial dimer. Below the micrograph, selected-area FFT patterns are shown corresponding to either the entire dimer or just the left or right QD. Lattice fringes and FFT analysis show that the QDs are epitaxially connected on the (100) facet.

(C) HRTEM micrograph of an epitaxial dimer with a twinning boundary at the attachment interface. See also Figure S9.

mean (Figure S6). We do not see evidence for such large QDs in TEM images (Figure 4A and previous publications[17,19]). However, we do occasionally see two QDs that appear to be touching each other. High-resolution TEM (HRTEM) reveals that some of these QD pairs are epitaxially fused QD dimers (Figures 4B and 4C), which are expected to have a lower energy than a single QD.[1,30]

Intentional formation of PbSe QD dimers during solution-phase synthesis has been demonstrated,[30] as has oriented attachment of PbSe QDs to form extended superlattices.[31,32] Removal of surface ligands using $(NH_4)_2S$ results in connected QD assemblies for PbS, PbSe, CdSe, and CdS QDs, indicating that bare QD surfaces likely attach across a range of materials.[33] It is therefore reasonable to expect that a few dimers could form unintentionally during standard synthesis and ligand-exchange procedures. Selective-area fast Fourier transform (FFT) analysis of the crystal fringes on each half of the QD dimer shown in Figure 4B reveals the relative orientation of the QDs, and their attached crystal facet (see the Supplemental Information and Figure S9 for more details). We observe fusing predominantly on the {100} facets in our QD dimers. Oriented attachment of PbSe QDs also proceeds along the {100} facets.[31,32] Increased likelihood of fusing on the {100} facet may be a result of more weakly bound ligands and a greater chance of a bare surface on this facet compared with the {111} facet.[34]

As shown in Figures 2E and 2J, trap states are already present before ligand exchange and are even observed in solution (Figure S7), indicating that some dimers are formed during the initial synthesis and handling. (Note, however, that this observation is specific to QDs synthesized via the lead choloride method; PbS QDs synthesized from lead acetate or lead oxide did not exhibit spectral signatures of the trap

state until after solid-state ligand exchange.) Previous work showed that intentionally prepared dimers are not separated from single QDs by size-selective precipitation using common solvent/non-solvent pairs,[30] so they are not likely to be removed during the usual purification steps. Based on comparison of the initial bleach intensity in Figures 2A–2E, we conclude that additional dimers are also formed during the solid-state ligand-exchange step, increasing the trap-state density by 50%–100% following ligand exchange. In samples made with QDs synthesized using lead oxide or lead acetate precursors in octadecene and oleic acid,[35–37] dimer trap states were not observed in QD solids with the native oleic acid ligands, but were observed following ligand exchange (Figure S8).

Hughes et al.[30] previously observed energetic splitting between the single QD and QD dimer levels, which decreased with increasing QD size from ~150 meV for 3-nm QDs to ~50 meV for 7-nm QDs.[30] This size-dependent trend in the energy splitting was explained using a tight binding model based on the effective mass approximation and spherical wave functions, with faceted QDs represented by spherical QDs of equivalent volume.[30,38] This model predicts slightly shallower trap-state depth than the ~100–200 meV we observe in our 4- to 5-nm faceted PbS QDs, but the size-dependent trend is consistent (Figure S6).

To elucidate the origin of the trap states, we performed DFT calculations. Prototype PbS QD (d = 2.0 nm) dimers fused along the {100} facet without surface ligands are considered in this work. A series of dimers were constructed to represent various degrees of fusing, as illustrated in Figure 5A, and their electronic structures and absorption spectra are compared with a single QD (Figures 5B–5D). The computed band gap (~1.0 eV) of our 2-nm QD is underestimated compared with experimental one due to the well-known DFT underestimation of semiconductor band gaps, although trends are typically well represented. In addition, the inclusion of spin-orbit coupling, which is important for describing the electronic structure of lead chalcogenide QDs, is known to further reduce the band gap.[39,40] The calculated band gaps of the dimers decrease as the fusing increases, which agrees with previous work in which the energy splitting increases as the overlap between the QDs increases.[30]

Figure 5B shows the absorption spectra calculated within the single-particle approximation. The first excitonic peaks of the dimers are generally red-shifted compared with the single QD, with the absorption coefficient on the same order of magnitude. Surprisingly, when two individual QDs are in direct contact (four atoms in the fusing plane), there is negligible shift in the first excitonic peak compared with the single QD. This is due to the small hybridization of the wavefunctions when the overlap is small. In fact, the calculated energy splitting between the symmetric and antisymmetric combinations of the highest occupied molecular orbital (HOMO) and lowest unoccupied molecular orbital (LUMO) of single QDs are less than 10 meV. As the degree of fusing increases to 12, 16, and 24 atoms in the fused plane, there is significant localization of the wavefunction around the fused region, creating new LUMO that are lower in energy than the LUMO of the single QD by around 80–160 meV, as shown in Figure 5C. Given the smaller computed band gap, the computed LUMO red-shifts for the dimers are in general agreement with our experimentally measured values of 150–200 meV. This new state is due to a quantum confinement effect in the fused region and cannot be explained using a simple picture of a linear combination of molecular orbitals from individual QDs. These results demonstrate that it is probably the dimer electron level that is shifted relative to neighboring individual dots, as the energies of the HOMO of the dimers are almost unchanged

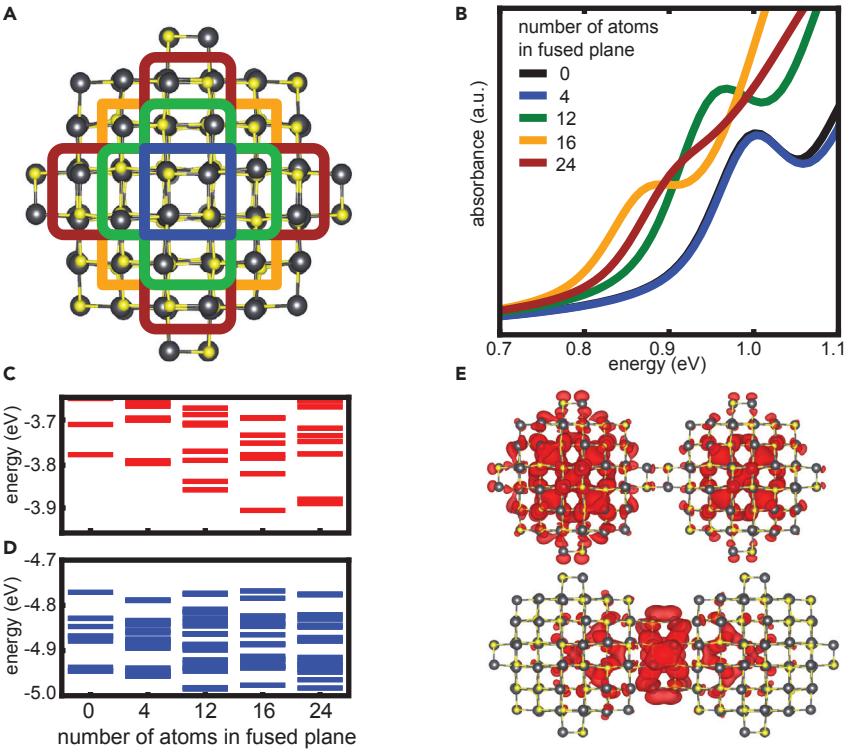

Figure 5. DFT Simulations of PbS QD Dimers

(A) Side view of the 2-nm diameter single PbS QD. Pb and S atoms are represented by black and yellow spheres, respectively. The colored boxes represent increasing degree of fusing in the QD dimers, from 4 (blue) to 12 (green), 16 (orange), and 24 (red) atoms. The fusing occurs along the {100} facet.

(B–D) The absorption spectra (B) and unoccupied orbital (C) and occupied orbital (D) energies of fused dimers, compared with a single isolated QD (0 fused atoms).

(E) The wavefunction of the LUMO of a dimer with 4 atoms in the fused plane (top) and 12 atoms in the fused plane (bottom).

See also Figure S10.

(Figure 5D). It should be noted that the energy shifts are not directly proportional to the degree of fusing; rather, they depend on the exact geometric configuration of the fused region.

We also calculated the electronic structures and absorption spectra for larger QDs (d = 2.5 nm) and their dimers (Figure S10). With a computed band gap of 0.7 eV for the single QD, the dimer LUMO states are around 25–50 meV lower in energy. As found in the case of smaller QDs, we observe wavefunction localization in the fused region once a significant degree of fusing (greater than 12 atoms in the fused plane) is introduced.

The energetic shifts attained in these atomistic calculations are consistent with the experimentally measured trap-state energies and with the expected size-dependent trend. The number of atoms in the attached facet adds another variable in addition to size dispersity that increases the energetic disorder of QD dimers in comparison with single QDs. Thus, we expect a greater linewidth for the ensemble QD dimer absorption compared with the single QD absorption, which is observed experimentally for the highly monodisperse QDs. The lowest energy transitions of QD dimers and the degeneracy and absorption cross-section of these transitions are consistent

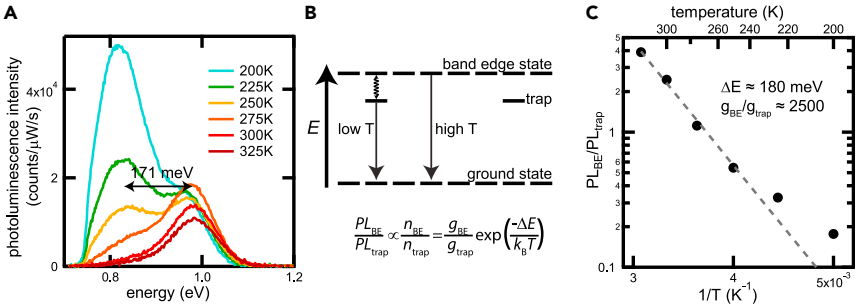

Figure 6. Emission from Band-Edge and Trap States in Ethanethiol-Treated PbS QD Solids

(A) PL spectra as a function of temperature showing PL from the band-edge state at room temperature and from the trap state at lower temperatures.

(B) Schematic showing much higher density of states at the band-edge than at the trap-state energy, so that at room temperature, charge-carrier occupation of band-edge states is entropically favored.

(C) Ratio of band-edge to trap-state PL as a function of temperature (filled circles). A fit (dashed line) gives the trap-state depth and density.

See also Figures S11 and S12.

with the assignment of trap states in QD solids to QD dimers fused on the {100} facets.

Charge-Carrier Equilibrium between Band Edge and Trap State

In Figure 6A, we present PL spectra of films of ethanethiol-capped 4.9-nm diameter QDs (1.08 eV first absorption peak). At room temperature, we observe emission from the band-edge state but, as the temperature decreases, emission from a spectrally distinct lower-energy state grows in. Similar sub-band emission has been observed in lead chalcogenide QDs in a variety of chemical environments.[41–44] Chuang et al. identified this state as the likely origin of the large open-circuit voltage deficit in PbS QD photovoltaics.[3] Although the trap state is lower in energy by an amount (~170 meV) many times greater than the available thermal energy at 300 K (~25 meV), the room-temperature emission spectrum is nonetheless dominated by the band edge. This is due to the much greater number of band-edge states than trap states, as shown in the schematic of Figure 6B. The PL intensity of each state is proportional to the occupation, n, which follows a Boltzmann distribution that accounts for the degeneracies, g, of the band-edge (BE) and trap states:

$$\frac{\mathrm{PL_{BE}}}{\mathrm{PL_{trap}}} \propto \frac{n_{\mathrm{BE}}}{n_{\mathrm{trap}}} = \frac{g_{\mathrm{BE}}}{g_{\mathrm{trap}}} \exp\left(\frac{-\Delta E}{k_{\mathrm{B}} T}\right), \qquad \text{(Equation 1)}$$

where ΔE is the difference in energy between the trap state and the band edge. If we assume similar radiative efficiency for the band-edge and trap states, the degeneracy ratio and trap-state depth can be found by fitting the data to Equation 1, as shown in Figure 6C. Note that this fit is valid only at high temperatures (T > 250 K) when charge transfer rates are sufficiently fast to establish equilibrium between the band-edge and trap-state manifolds.[45,46] A fit to the data yields a trap-state degeneracy of 1 in ~2,500 QDs, which is consistent with other published trap-state densities in thiol-treated films measured using a variety of techniques.[4,10,11,15,47] The fitted activation energy of ~180 meV is approximately equal to the energy difference between the band gap and trap-state PL features, further reinforcing the assumption of equilibrium which is implicit in the use of Equation 1.

To further confirm that thermal equilibrium between band-edge states and trap states can be established with a trap-state density of 1 in ~2,500 QDs, we performed

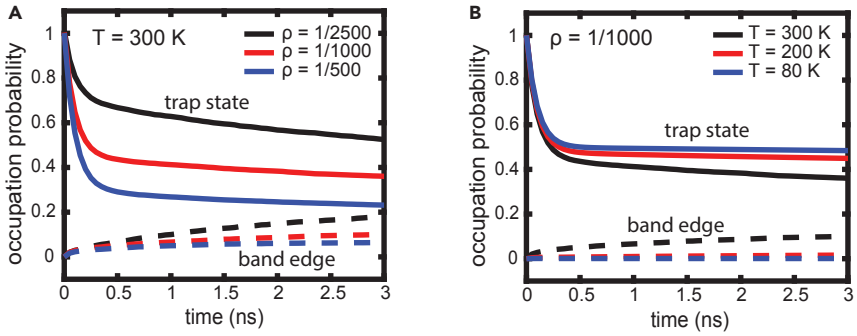

Figure 7. Kinetic Monte Carlo Simulations for Detrapping Kinetics at Various Temperatures and Trap Densities

(A) Occupation probability of the band-edge state and the trap state as a function of time at various trap-state densities.

(B) Occupation probability of the band-edge state and the trap state as a function of time at different temperatures.

See also Table S1.

KMC simulations in model QD solids with different trap-state densities at various temperatures. In our model, we follow a free carrier (electron or hole) undergoing a series of stochastic hops between individual QDs. We describe the hopping rate using the Miller-Abrahams rate equations (see Experimental Procedures for more details). To highlight the temperature-activated charge-carrier detrapping dynamics, we assume the hopping rate prefactor, as well as other material-specific parameters, to be temperature independent. These simulations include fast recombination through the trap state (contributing to the simulated trap-state population dynamics), but do not include the Auger-assisted detrapping pathway. Figure 7A explores the effect of trap-state density on the occupation probability at T = 300 K. At lower trap-state density more uphill thermalization is observed, which is consistent with the experimentally observed entropically driven detrapping mechanism. In Figure 7B, we simulate the effect of temperature on the occupation probability of the band-edge and trap states. Growth of the band-edge state occupancy is observed within the simulation time window at 300 K but not at lower temperatures, which is consistent with the thermally activated hopping mechanism and associated experimental data shown in Figure 3.

Conclusions and Outlook

In light of the assignment of traps in PbS QD solids to QD dimers, we re-examined the literature, which has generally assigned trap states to QD surfaces. Changes in the trap-state density as a result of different ligand treatments[9,10] may reflect a change in the likelihood of QD fusing, rather than the creation of surface defects. Bozyigit et al.[48] used thermal admittance spectroscopy to measure the spectrum of electronic trap states in PbS QD solids, and found a trap-state spectrum that looks similar to a QD absorption spectrum, consistent with our findings from atomistic simulations of QD dimers. Speirs et al.[49] observed a reduced trap-state density and 147-meV increase in the open-circuit voltage in PbS QD solar cells following overgrowth of a CdS shell. We propose that the CdS shell achieves these results by preventing dimer formation, rather than by passivating surface defects. Furthermore, in light of the detrapping mechanisms we have observed (Figure 3F), the observation of electrical current in response to optical excitation below the band edge may result from charge-carrier detrapping and transport through band-edge states, rather than transport through mid-gap states.[5]

Future efforts must carefully optimize QD synthesis and device fabrication procedures to avoid the accidental formation of dimers, as they can significantly inhibit QD device performance even at very low concentrations of 1 in ~1,000 QDs. Improved separation techniques beyond size-selective precipitations are needed to remove dimers that form during synthesis. Since additional dimers also readily form during solid-state ligand exchange, solution-phase ligand exchanges,[50,51] followed by purification to remove any dimers, may be required to form strongly coupled QD solids free of dimer trap states that can ultimately boost QD device efficiency.

Finally, we acknowledge that there may be additional trap states that affect electrical device measurements that cannot be characterized using the optical techniques demonstrated here. Photoluminescence and absorption are sensitive only to states with non-vanishing transition dipole moment. Charge-separated states, such as electron or hole surface traps, may affect QD device efficiency but may not be observable using the techniques employed in this study.

EXPERIMENTAL PROCEDURES

PbS QD Synthesis and QD Solids Preparation

The 4.2-nm QDs were synthesized according to Zhang et al.[18] and the 4.9-nm QDs were synthesized according to Weidman et al.[17] Both syntheses use $PbCl_2$ in oleylamine, but the Zhang synthesis uses bis(trimethylsilyl)sulfide ($(TMS)_2S$) while the Weidman synthesis uses elemental sulfur. The native oleylamine ligands were replaced with oleic acid (oleate) ligands during purification steps following synthesis. Purified QDs were redispersed in toluene at a concentration of 100 mg/mL in a nitrogen glovebox. Forty microliters of this solution was spin cast at 1,500 rpm for 30 s onto a 0.5-inch square borosilicate glass slide (Schott D-263 from Thermo Fisher) that had been cleaned and treated overnight with 0.02 M (3-mercaptopropyl)trimethoxysilane (Sigma-Aldrich, 95%) solution in toluene to improve QD adhesion. Some samples were then placed in a 0.1 M solution of the desired ligand (1-ethanethiol [Sigma-Aldrich, 97%], 1-butanethiol [Sigma-Aldrich, 99%], 1-octanethiol [Sigma-Aldrich, 98.5%], 1-dodecanethiol [Sigma-Aldrich, ≥98%], or 3-mercaptopropionic acid [Sigma-Aldrich, ≥99%]) in acetonitrile for 24 h for ligand exchange. The ligand exchange for tetrabutylammonium iodide (Sigma-Aldrich, ≥99%) was done at a concentration of 10 mg/mL in methanol, and allowed to sit on the sample for 30 s before spinning to remove and then washing with pure methanol. This created films that were ~100–200 nm thick had an optical density of ~0.1 at the first absorption peak. Prior to ligand exchange, the QDs are air stable. Following ligand exchange, the samples were kept in an inert environment at all times, including during TA and PL measurements.

Photoluminescence Spectroscopy

PL spectra were collected using a 785-nm narrow-band continuous-wave diode laser. PL spectra were collected in a Janis ST-100 cryostat, which was loaded inside the glovebox to prevent air exposure. The laser was focused onto the sample using a 125-mm lens at ~30° from the normal, and emitted light was collected using a backscattered geometry with a 75-mm lens and sent to a Bayspec near-infrared spectrometer. The total power density was 0.2 W/cm^2 at the sample.

Transient Absorption Spectroscopy

TA spectroscopy was performed at the Advanced Optical Spectroscopy and Microscopy Facility at the Center for Functional Nanomaterials at Brookhaven National Laboratory. A commercial Ti:sapphire femtosecond regenerative amplifier

(SpectraPhysics Spitfire Pro) operating at a 1-kHz repetition rate was used to generate 800 nm fundamental. An optical parametric amplifier (LightConversion) was used to generate infrared pump pulses (1,150 nm, 1,200 nm, 1,250 nm, or 1,350 nm) with ~100 fs time resolution. A long-pass filter (Thorlabs) 50 nm shorter than the pump pulse wavelength (e.g., 1,200 nm long pass for 1,250-nm pump) was used to clean up the pump line to ensure it did not inadvertently excite higher-energy states. The probe pulses were generated by focusing a small portion of the 800-nm fundamental onto a sapphire crystal to generate a white-light supercontinuum over the range of 850–1,600 nm. The probe light was split into signal and reference beams, which were detected on a shot-by-shot basis by fiber-coupled InGaAs diode arrays coupled to a high-speed data-acquisition system (Ultrafast Systems). The pump-probe time delay was controlled by a mechanical delay stage (Newport). Each measurement is an average of several scans of the delay stage to ensure that dynamics were not changing with laser exposure time. Probe power was typically only a few hundred nanowatts. The pump power to excite the trap state was 300 μW to 2.7 mW, but a significant portion of this light was scattered or transmitted through the sample because the trap-state density is low and, as a result, the absorbance at those wavelengths is low.

Transmission Electron Microscopy

TEM was performed on a JEOL 2011 instrument operating at 200 kV. HRTEM images were collected on a JEOL 2010 instrument operating at 200 kV. Samples were prepared by drop casting QD suspensions in hexanes onto copper TEM grids coated with an amorphous carbon support film.

Photothermal Deflection Spectroscopy

PDS was performed according to Jean et al.[24] In brief, the QDs were deposited on custom 4 × 12-mm fused quartz slivers. The pump beam consists of a 300-W Xe arc lamp chopped at 10 Hz, a dual-grating monochromator with 1-mm slits, a periscope, and achromatic lenses to collimate and focus the beam. The sample film was secured using a custom holder in a standard 10-mm quartz cuvette. The probe beam consists of a 658-nm, 40-mW temperature-controlled laser diode, an anamorphic prism pair, spatial filter, and iris to circularize the beam and isolate the fundamental mode; a band-pass filter to eliminate scattered light; and a quadrant detector with built-in transimpedance amplifier.

Density Functional Theory Calculations

All DFT calculations were performed using the Vienna Ab Initio Simulation Package (VASP, v5.4.4).[52,53] The semi-local Perdew-Burke-Ernzerhof generalized gradient approximation[54] is used for the exchange correlation functional. Electronic wavefunctions were expanded in plane-waves basis with an energy cutoff of 400 eV. The Pb $5d^{10}6s^26p^2$ and S $3s^23p^6$ electrons were included in the valence, and the core-valence interaction was treated by the projector-augmented wave method.[55] Spin-orbit coupling effects were included for all atoms.[56] A vacuum spacing of 15 Å was added to the supercell in all three spatial directions to remove any spurious interactions, and only gamma k-point was sampled. The total energies were converged to 10^{-6} eV and the atomic positions were relaxed until the residual forces were less than 0.01 eV/Å. The frequency-dependent dielectric function was computed using the independent particle approximation. The absorption coefficient, $\alpha(\omega)$, was obtained using the formula $\alpha(\omega) = \frac{\omega}{cn(\omega)}\varepsilon_2(\omega)$, where c is the speed of light in vacuum, $\varepsilon_2(\omega)$ is the imaginary part of the dielectric function, and $n(\omega)$ is the real part of the complex refractive index, $n^2(\omega) = \frac{1}{2}(\varepsilon_1 + \sqrt{\varepsilon_2^2 + \varepsilon_1^2})$, with $\varepsilon_1(\omega)$ the real

part of the dielectric function. Electronic wavefunctions were visualized using the VESTA program.[57]

Kinetic Monte Carlo Simulations

Numerical simulations of carrier transport in QD solids were performed using a KMC algorithm in which a free carrier (electron or hole) undergoes a series of stochastic hops between individual quantum dots. The hopping rate for electrons in the conduction band and holes in the valence band from QD *i* to QD *j* was specified using the Miller-Abrahams rate equation

$$k_{ji}^{(\alpha)} = \begin{cases} k^{(\alpha)} \exp\left(-\frac{(\varepsilon_j - \varepsilon_i)/2}{k_B T} \right); & \varepsilon_j > \varepsilon_i \\ k^{(\alpha)} \quad ; & \varepsilon_j \leq \varepsilon_i \end{cases}, \qquad \text{(Equation 2)}$$

where $k^{(\alpha)}$ is the hopping rate prefactor of a free charge carrier (α = "–" or "+" for an electron or hole, respectively), ε_i is the energy of the *i*th QD, k_B is the Boltzmann constant, and T is the temperature. The factor of $^1/_2$ in the exponential arises from the assumption of equal sharing of the inhomogeneous distribution of band-gap energies between conduction and valence band levels. Here we assume that the hopping rate prefactor is constant over the temperature range we observe to highlight the phenomenon of temperature-activated charge-carrier dynamics from trap to band-edge states. Therefore, we assumed that material-specific parameters, such as absorption peak energies ($\bar{\varepsilon}$), energetic disorder (σ_{ih}), and QD superlattice structure, in the KMC model remain constant (see Table S1). The QD solid model consists of a three-dimensional periodically replicated cell in a body-centered cubic lattice configuration containing N = 32,000 QDs with a fractional trap-state density, ρ = (number of trap states)/N. Each QD is randomly assigned either a band-edge absorption energy or a trap-state absorption energy, drawn from a Gaussian distribution with a standard deviation, σ_{inh}, and a peak absorption energy, ($\bar{\varepsilon}$). For details on the KMC model procedure and parameterization of QD samples, see Supplemental Information.

SUPPLEMENTAL INFORMATION

Supplemental Information can be found online at https://doi.org/10.1016/j.matt.2019.05.015.

ACKNOWLEDGMENTS

We thank M. Sfeir for assistance with TA measurements and M. Nasilowski for QDs synthesized with lead oxide and lead acetate. This work was supported by the US Department of Energy (DOE), Office of Basic Energy Sciences, under award number DE-SC0010538. W.A.T. received partial support from DE-SC0019345. W.S.W. was supported by the US National Science Foundation under award no. 1452857. E.M.Y.L. was supported by an NSF Graduate Research Fellowship under grant no. 1122374. Y.L. acknowledges the financial support by National Science Scholarship from Singapore. This research used resources of the Center for Functional Nanomaterials, which is a US DOE Office of Science Facility, at Brookhaven National Laboratory under contract no. DE-SC0012704. This research used the computational resources of the National Energy Research Scientific Computing Center, a DOE Office of Science User Facility supported by the Office of Science of the US DOE under contract no. DE-AC02-05CH11231 and Extreme Science and Engineering Discovery Environment (XSEDE), which is supported by National Science Foundation grant number ACI-1053575.

AUTHOR CONTRIBUTIONS

R.H.G. conceived the project, prepared samples, and collected and analyzed TA and photoluminescence data with assistance from W.S.-W. under the supervision of W.A.T. N.S.D. collected and analyzed TEM images. M.C.W. synthesized QDs and advised on TEM analysis. Y.L. performed DFT calculations and analyzed computational results with input from H.L. under the supervision of J.C.G. E.M.Y.L. performed KMC calculations and analyzed results under the supervision of A.P.W. J.J. and W.S.-W. collected and analyzed photothermal deflection spectroscopy data under the supervision of V.B. R.H.G., W.S.W., and W.A.T. wrote the manuscript with contributions from the other authors.

DECLARATION OF INTERESTS

The authors declare no competing interests.

Received: March 22, 2019
Revised: May 5, 2019
Accepted: May 10, 2019
Published: July 10, 2019

REFERENCES

1. Guyot-Sionnest, P. (2012). Electrical transport in colloidal quantum dot films. J. Phys. Chem. Lett. *3*, 1169–1175.

2. Kagan, C.R., and Murray, C.B. (2015). Charge transport in strongly coupled quantum dot solids. Nat. Nanotechnol. *10*, 1013–1026.

3. Chuang, C.H.M., Maurano, A., Brandt, R.E., Hwang, G.W., Jean, J., Buonassisi, T., Bulović, V., and Bawendi, M.G. (2015). Open-circuit voltage deficit, radiative sub-bandgap states, and prospects in quantum dot solar cells. Nano Lett. *15*, 3286–3294.

4. Zhitomirsky, D., Voznyy, O., Levina, L., Hoogland, S., Kemp, K.W., Ip, A.H., Thon, S.M., and Sargent, E.H. (2014). Engineering colloidal quantum dot solids within and beyond the mobility-invariant regime. Nat. Commun. *5*, 3803.

5. Nagpal, P., and Klimov, V.I. (2011). Role of mid-gap states in charge transport and photoconductivity in semiconductor nanocrystal films. Nat. Commun. *2*, 486.

6. Zhang, Y., Zherebetskyy, D., Bronstein, N.D., Barja, S., Lichtenstein, L., Schuppisser, D., Wang, L.W., Alivisatos, A.P., and Salmeron, M. (2015). Charge percolation pathways guided by defects in quantum dot solids. Nano Lett. *15*, 3249–3253.

7. Gao, J., Nguyen, S.C., Bronstein, N.D., and Alivisatos, A.P. (2016). Solution-processed, high-speed, and high-quantum-efficiency quantum dot infrared photodetectors. ACS Photon. *3*, 1217–1222.

8. Bakulin, A.A., Neutzner, S., Bakker, H.J., Ottaviani, L., Barakel, D., and Chen, Z. (2013). Charge trapping dynamics in PbS colloidal quantum dot photovoltaic devices. ACS Nano *7*, 8771–8779.

9. Ip, A.H., Thon, S.M., Hoogland, S., Voznyy, O., Zhitomirsky, D., Debnath, R., Levina, L., Rollny, L.R., Carey, G.H., Fischer, A., et al. (2012). Hybrid passivated colloidal quantum dot solids. Nat. Nanotechnol. *7*, 577–582.

10. Wanger, D.D., Correa, R.E., Dauler, E.A., and Bawendi, M.G. (2013). The dominant role of exciton quenching in PbS quantum-dot-based photovoltaic devices. Nano Lett. *13*, 5907–5912.

11. Bozyigit, D., Volk, S., Yarema, O., and Wood, V. (2013). Quantification of deep traps in nanocrystal solids, their electronic properties, and their influence on device behavior. Nano Lett. *13*, 5284–5288.

12. Hwang, G.W., Kim, D., Cordero, J.M., Wilson, M.W.B., Chuang, C.-H.M., Grossman, J.C., and Bawendi, M.G. (2015). Identifying and eliminating emissive sub-bandgap states in thin films of pbs nanocrystals. Adv. Mater. *27*, 4481–4486.

13. Ip, A.H., Kiani, A., Kramer, I.J., Voznyy, O., Movahed, H.F., Levina, L., Adachi, M.M., Hoogland, S., and Sargent, E.H. (2015). Infrared colloidal quantum dot photovoltaics via coupling enhancement and agglomeration suppression. ACS Nano *9*, 8833–8842.

14. Li, H., Zhitomirsky, D., Dave, S., and Grossman, J.C. (2016). Toward the ultimate limit of connectivity in quantum dots with high mobility and clean gaps. ACS Nano *10*, 606–614.

15. Zhitomirsky, D., Voznyy, O., Hoogland, S., and Sargent, E.H. (2013). Measuring charge carrier diffusion in coupled colloidal quantum dot solids. ACS Nano *7*, 5282–5290.

16. Hughes, B.K., Blackburn, J.L., Kroupa, D., Shabaev, A., Erwin, S.C., Efros, A.L., Nozik, A.J., Luther, J.M., and Beard, M.C. (2014). Synthesis and spectroscopy of PbSe fused quantum-dot dimers. J. Am. Chem. Soc. *136*, 4670–4679.

17. Weidman, M.C., Beck, M.E., Hoffman, R.S., Prins, F., and Tisdale, W.A. (2014). Monodisperse, air-stable pbs nanocrystals via precursor stoichiometry control. ACS Nano *8*, 6363–6371.

18. Zhang, J., Gao, J., Miller, E.M., Luther, J.M., and Beard, M.C. (2014). Diffusion-controlled synthesis of PbS and PbSe quantum dots with in situ halide passivation for quantum dot solar cells. ACS Nano *8*, 614–622.

19. Weidman, M.C., Yager, K.G., and Tisdale, W.A. (2015). Interparticle spacing and structural ordering in superlattice PbS nanocrystal solids undergoing ligand exchange. Chem. Mater. *27*, 474–482.

20. Gilmore, R.H., Lee, E.M.Y., Weidman, M.C., Willard, A.P., and Tisdale, W.A. (2017). Charge carrier hopping dynamics in homogeneously broadened PbS quantum dot solids. Nano Lett. *17*, 893–901.

21. An, J.M., Franceschetti, A., and Zunger, A. (2007). The excitonic exchange splitting and radiative lifetime in PbSe quantum dots. Nano Lett. *7*, 2129–2135.

22. Gao, J., and Johnson, J.C. (2012). Charge trapping in bright and dark states of coupled PbS quantum dot films. ACS Nano *6*, 3292–3303.

23. Erslev, P.T., Chen, H.Y., Gao, J.B., Beard, M.C., Frank, A.J., van de Lagemaat, J., Johnson, J.C., and Luther, J.M. (2012). Sharp exponential band tails in highly disordered lead sulfide quantum dot arrays. Phys. Rev. B *86*, 155313.

24. Jean, J., Mahony, T.S., Bozyigit, D., Sponseller, M., Holovský, J., Bawendi, M.G., and Bulović, V. (2017). Radiative efficiency limit with band tailing exceeds 30% for quantum dot solar cells. ACS Energy Lett. *2*, 2616–2624.

25. Klimov, V.I. (2007). Spectral and dynamical properties of multiexcitons in semiconductor nanocrystals. Annu. Rev. Phys. Chem. *58*, 635–673.

26. Trinh, M.T., Sfeir, M.Y., Choi, J.J., Owen, J.S., and Zhu, X. (2013). A hot electron-hole pair breaks the symmetry of a semiconductor quantum dot. Nano Lett. *13*, 6091–6097.

27. Cademartiri, L., Montanari, E., Calestani, G., Migliori, A., Guagliardi, A., and Ozin, G.A. (2006). Size-dependent extinction coefficients of PbS quantum dots. J. Am. Chem. Soc. *128*, 10337–10346.

28. Zhu, H., Yang, Y., Hyeon-Deuk, K., Califano, M., Song, N., Wang, Y., Zhang, W., Prezhdo, O.V., and Lian, T. (2014). Auger-assisted electron transfer from photoexcited semiconductor quantum dots. Nano Lett. *14*, 1263–1269.

29. Olshansky, J.H., Ding, T.X., Lee, Y.V., Leone, S.R., and Alivisatos, A.P. (2015). Hole transfer from photoexcited quantum dots: the relationship between driving force and rate. J. Am. Chem. Soc. *137*, 15567–15575.

30. Hughes, B.K., Blackburn, J.L., Kroupa, D., Shabaev, A., Erwin, S.C., Efros, A.L., Nozik, A.J., Luther, J.M., and Beard, M.C. (2014). Synthesis and spectroscopy of PbSe fused quantum-dot dimers. J. Am. Chem. Soc. *136*, 4670–4679.

31. Geuchies, J.J., van Overbeek, C., Evers, W.H., Goris, B., de Backer, A., Gantapara, A.P., Rabouw, F.T., Hilhorst, J., Peters, J.L., Konovalov, O., et al. (2016). In situ study of the formation mechanism of two-dimensional superlattices from PbSe nanocrystals. Nat. Mater. *15*, 1248–1254.

32. Whitham, K., Yang, J., Savitzky, B.H., Kourkoutis, L.F., Wise, F., and Hanrath, T. (2016). Charge transport and localization in atomically coherent quantum dot solids. Nat. Mater. *15*, 557–563.

33. Zhang, H., Hu, B., Sun, L., Hovden, R., Wise, F.W., Muller, D.A., and Robinson, R.D. (2011). Surfactant ligand removal and rational fabrication of inorganically connected quantum dots. Nano Lett. *11*, 5356–5361.

34. Choi, J.J., Bealing, C.R., Bian, K., Hughes, K.J., Zhang, W., Smilgies, D.M., Hennig, R.G., Engstrom, J.R., and Hanrath, T. (2011). Controlling nanocrystal superlattice symmetry and shape-anisotropic interactions through variable ligand surface coverage. J. Am. Chem. Soc. *133*, 3131–3138.

35. Hines, M.A., and Scholes, G.D. (2003). Colloidal PbS nanocrystals with size-tunable near-infrared emission: observation of post-synthesis self-narrowing of the particle size distribution. Adv. Mater. *15*, 1844–1849.

36. Zhao, N., Osedach, T.P., Chang, L.Y., Geyer, S.M., Wanger, D., Binda, M.T., Arango, A.C., Bawendi, M.G., and Bulović, V. (2010). Colloidal PbS quantum dot solar cells with high fill factor. Acs Nano *4*, 3743–3752.

37. Chuang, C.H.M., Brown, P.R., Bulović, V., and Bawendi, M.G. (2014). Improved performance and stability in quantum dot solar cells through band alignment engineering. Nat. Mater. *13*, 796–801.

38. Shabaev, A., Efros, A.L., and Efros, A.L. (2013). Dark and photo-conductivity in ordered array of nanocrystals. Nano Lett. *13*, 5454–5461.

39. Hummer, K., Grüneis, A., and Kresse, G. (2007). Structural and electronic properties of lead chalcogenides from first principles. Phys. Rev. B *75*, 195211.

40. Wei, S.-H., and Zunger, A. (1997). Electronic and structural anomalies in lead chalcogenides. Phys. Rev. B *55*, 13605–13610.

41. Caram, J.R., Bertram, S.N., Utzat, H., Hess, W.R., Carr, J.A., Bischof, T.S., Beyler, A.P., Wilson, M.W.B., and Bawendi, M.G. (2016). PbS nanocrystal emission is governed by multiple emissive states. Nano Lett. *16*, 6070–6077.

42. Yue, F., Tomm, J.W., and Kruschke, D. (2014). Experimental observation of exciton splitting and relaxation dynamics from PbS quantum dots in a glass matrix. Phys. Rev. B *89*, 081303.

43. Harbold, J.M., and Wise, F.W. (2007). Photoluminescence spectroscopy of PbSe nanocrystals. Phys. Rev. B *76*, 125304.

44. Grodzinska, D., Evers, W.H., Dorland, R., van Rijssel, J., van Huis, M.A., Meijerink, A., Donega, C.D., and Vanmaekelbergh, D. (2011). Two-fold emission from the S-shell of PbSe/CdSe core/shell quantum dots. Small *7*, 3493–3501.

45. Zhang, J., Tolentino, J., Smith, E.R., Zhang, J., Beard, M.C., Nozik, A.J., Law, M., and Johnson, J.C. (2014). Carrier transport in PbS and PbSe QD films measured by photoluminescence quenching. J. Phys. Chem. C *118*, 16228–16235.

46. Gao, J., Zhang, J., van de Lagemaat, J., Johnson, J.C., and Beard, M.C. (2014). Charge generation in PbS quantum dot solar cells characterized by temperature-dependent steady-state photoluminescence. ACS Nano *8*, 12814–12825.

47. Bozyigit, D., Lin, W.M.M., Yazdani, N., Yarema, O., and Wood, V. (2015). A quantitative model for charge carrier transport, trapping and recombination in nanocrystal-based solar cells. Nat. Commun. *6*, 6180.

48. Bozyigit, D., Yazdani, N., Yarema, M., Yarema, O., Lin, W.M.M., Volk, S., Vuttivorakulchai, K., Luisier, M., Juranyi, F., and Wood, V. (2016). Soft surfaces of nanomaterials enable strong phonon interactions. Nature *531*, 618–622.

49. Speirs, M.J., Balazs, D.M., Fang, H.H., Lai, L.H., Protesescu, L., Kovalenko, M.V., and Loi, M.A. (2015). Origin of the increased open circuit voltage in PbS-CdS core-shell quantum dot solar cells. J. Mater. Chem. A. *3*, 1450–1457.

50. Lin, Q., Yun, H.J., Liu, W., Song, H.J., Makarov, N.S., Isaienko, O., Nakotte, T., Chen, G., Luo, H., Klimov, V.I., and Pietryga, J.M. (2017). Phase-transfer ligand exchange of lead chalcogenide quantum dots for direct deposition of thick, highly conductive films. J. Am. Chem. Soc. *139*, 6644–6653.

51. Liu, M., Voznyy, O., Sabatini, R., Garcia de Arquer, F.P., Munir, R., Balawi, A.H., Lan, X., Fan, F., Walters, G., Kirmani, A.R., et al. (2017). Hybrid organic-inorganic inks flatten the energy landscape in colloidal quantum dot solids. Nat. Mater. *16*, 258–263.

52. Kresse, G., and Furthmüller, J. (1996). Efficient iterative schemes for ab initio total-energy calculations using a plane-wave basis set. Phys. Rev. B *54*, 11169–11186.

53. Kresse, G., and Furthmüller, J. (1996). Efficiency of ab-initio total energy calculations for metals and semiconductors using a plane-wave basis set. Comput. Mater. Sci. *6*, 15–50.

54. Perdew, J.P., Burke, K., and Ernzerhof, M. (1996). Generalized gradient approximation made simple. Phys. Rev. Lett. *77*, 3865–3868.

55. Kresse, G., and Joubert, D. (1999). From ultrasoft pseudopotentials to the projector augmented-wave method. Phys. Rev. B *59*, 1758–1775.

56. Steiner, S., Khmelevskyi, S., Marsmann, M., and Kresse, G. (2016). Calculation of the magnetic anisotropy with projected-augmented-wave methodology and the case study of disordered $Fe_{1-x}Co_x$ alloys. Phys. Rev. B *93*, 224425.

57. Momma, K., and Izumi, F. (2008). VESTA: a three-dimensional visualization system for electronic and structural analysis. J. Appl. Cryst. *41*, 653–658.